Controlling the Phase Transition in Nanocrystalline Ferroelectric Thin Films via Cation Ratio

Journal:	*Nanoscale*
Manuscript ID	NR-ART-08-2018-006268.R1
Article Type:	Paper
Date Submitted by the Author:	21-Sep-2018
Complete List of Authors:	Golovina, Iryna; Drexel University, Materials Science + Engineering Falmbigl, Matthias; Institute of Physical Chemistry, University of Vienna Hawley, Christopher; Drexel University, Materials Science + Engineering Ruffino, Anthony; Drexel University, Physics Plokhikh, Aleksandr; Drexel University, Materials Science + Engineering Karateev, Igor; Kurchatov Institute Parker, Thomas; US Army Research Laboratory Gutierrez-Perez, Alejandro; Drexel University, Materials Science + Engineering Vasiliev, Alexander; Russian Research Centre "Kurchatov Institute", NBIC Spanier, Jonathan; Drexel University, Materials Science + Engineering

Nanoscale

PAPER

Controlling the Phase Transition in Nanocrystalline Ferroelectric Thin Films via Cation Ratio

Received 00th January 20xx,
Accepted 00th January 20xx

DOI: 10.1039/x0xx00000x

www.rsc.org/

Iryna S. Golovina,[a] Matthias Falmbigl,[a] Christopher J. Hawley,[a,b] Anthony J. Ruffino,[a] Aleksandr V. Plokhikh,[a] Igor A. Karateev,[c] Thomas C. Parker,[d] Alejandro Gutierrez-Perez,[a] Alexandre L. Vasiliev [d] and Jonathan E. Spanier [*a,e,f]

Traditionally, the ferroelectric Curie temperature can be manipulated by chemical substitution, *e.g.*, in $Ba_{1-x}Sr_xTiO_3$ as one of the archetypical representatives. Here, we show a novel approach to tune the ferroelectric phase transition applicable for nanostructured thin films. We demonstrate this effect in nano-grained $BaTiO_3$ films. Based on an enhanced metastable cation solubility with Ba/Ti-ratios of 0.8 to 1.06, a significant shift of the phase transition temperature is discovered. The transition temperature increases linearly from 212 K to 350 K with increasing Ba/Ti ratio. For all Ba/Ti ratios, a completely diffused phase transition is present resulting in a negligible temperature sensitivity of the dielectric constant. Schottky defects are identified as the driving force behind the off-stoichiometry and the shift of the phase transition temperature as they locally induce lattice strain. Complementary temperature dependent Raman experiments reveal the presence of the hexagonal polymorph in addition to the perovskite phase in all cases. Interestingly, the hexagonal $BaTiO_3$ influences the structural transformation on the Ba-rich side, while on the Ti-rich side no changes for the hexagonal polymorph at the ferroelectric transition temperature are observed. This concerted structural change of both polymorphs on the Ba-rich side causes a broad phase transition region spanning over a wide range up to 420 K including the transition temperature of 350 K obtained from dielectric measurements. These findings are promising for fine adjustment of the phase transition temperature and low temperature coefficient of permittivity.

Introduction

The ferroelectric phase transition is a cooperative phenomenon, where tuning of the Curie temperature (T_C) is crucial for many practical applications, including high-density memory devices (FeRAM),[1,2] wireless power transfer (WPT) systems,[3,4] tunable microwave devices,[5] and surface acoustic wave (SAW) resonators.[6] Traditionally, two approaches are used to control T_C, including the type of the ferroelectric phase: doping and finite-size scaling. Regardless of the approach, the effects arise from strain of different origins. Initially, the T_C in ferroelectric oxides was manipulated by chemical substitution. Among others, the most prominent examples are solid solutions of $(Ba,Sr)TiO_3$ (BST),[7,8] $Pb(Zr,Ti)O_3$ (PZT),[9,10] $K(Ta,Nb)O_3$ (KTN),[11,12] where the T_C can shift up to 400 K in bulk materials between the two end members due to complete solubility of dopants. In this case, the critical concentration of dopants provokes certain structural changes and drives T_C higher or lower, depending on the particular dopant and resulting lattice instability. Rapid development of nanotechnology for ferroelectrics over the past decades revealed a number of scaling effects, which appeared to considerably influence T_C. Size effects are tentatively classified as "extrinsic" and "intrinsic" size effects. Extrinsic size effects encompass the contribution of surface stress, surface bond contraction and Vegard strains/stresses. In 3D nanocrystals, extrinsic effects lead to a shift of the Curie temperature proportional to either $1/R$[13–17] or $1/R^2$,[18,19] depending on the model, where R is the curvature radius of the nanoparticles surface. Intrinsic size effects arise from depolarization, correlation, and spontaneous flexoelectric effects.[20-22] More recently 2D thin-film studies revealed the influence of the film thickness[23-25] and interface (substrate-ferroelectric[25,26] and electrode-ferroelectric[27,28]) phenomena on the polarization variation and consequent changes in the ferroelectric phase transition behaviour. In general, the Curie temperature decreases with decreasing film thickness in order to balance the energy costs associated with long-range electrostatic effects (depolarization fields) with the formation of domain walls.[23] However, flexoelectricity, lattice relaxation and epitaxial strain may enhance surface polarization and lead to the

[a] Department of Materials Science & Engineering, Drexel University, Philadelphia, Pennsylvania 19104, USA. E-mail: spanier@drexel.edu
[b] Department of Physics, Lafayette College, Easton PA 18042, USA
[c] National Research Center "Kurchatov Institute", Kurchatov Square 1, Moscow 123182, Russia.
[d] US Army Research Laboratory, Aberdeen Proving Ground, Maryland 21005, USA.
[e] Department of Electrical & Computer Engineering, Drexel University, Philadelphia, Pennsylvania 19104, USA
[f] Department of Physics, Drexel University, Philadelphia, Pennsylvania 19104, USA

† Electronic Supplementary Information (ESI) available: The grain sizes distribution obtained from TEM study for all samples studied; the XPS Ti and Ba spectra for the films with Ba/Ti =0.8, 0.92, 1.01 and 1.06; the temperature dependence of the frequency, integrated intensity and FWHM of the 620 cm^{-1} phonon peak of the Raman spectra for the Ti-rich sample (Ba/Ti=0.8). See DOI: 10.1039/x0xx00000x

increase of T_C with decreasing film thickness.[24-26] For ferroelectric-electrode systems, the size-effect problem is described by the effective screening length (embodying the long-range electrostatic response of the interface) and the quadratic surface energy coefficient (embodying the short-range chemical interactions at the interface).[27] In ferroelectric nanowires, T_C is depressed as the nanowire diameter d_{nw} decreases, following a $1/d_{nw}$ scaling,[30] while the T_C could be higher in nanotubes compared to the bulk material for a negative electrostriction coefficient.[30] Finally, three dimensionally-confined ferroelectric nanostructures (nano/quantum dots) undergo an unusual phase transition - from a state exhibiting a spontaneous polarization to a phase associated with a toroid moment of polarization.[31,32] A combination of both approaches, doping and scaling, is also applicable. For example, impurity defect driven new phase states have been revealed in $KTaO_3$ and $KNbO_3$ nanoparticles.[33-35]

The effect of non-stoichiometry has not been exploited to the same extend for bulk materials as well as nanostructures with lower dimensionality. There are a few reports discussing the influence of the Ba/Ti ratio on T_C in $BaTiO_3$ (BTO) ceramics.[36-38] Lee *et al*. show that T_C decreases with increasing concentration of partial Schottky defects on both, the Ti- and the Ba-rich side.[38] In this work, the Ba/Ti ratio ranges from 0.93 to 1.04 and T_C varies with defect concentration by -2.2 K/δ for $Ba_{1-\delta}TiO_{3-\delta}$ and by −8.2 K/δ for $BaTi_{1-\delta}O_{3-2\delta}$. The authors further demonstrate the strong sensitivity of the Landau coefficients characterizing the properties of the monodomain ferroelectric state to non-stoichiometry involving partial Schottky disorder reactions in the perovskite-structured oxides.[37] W.P. Chen *et al*. show that with increasing Ba/Ti ratio from 0.96 to 1.04, the tetragonal distortion in the perovskite diminishes and the Curie point decreases monotonously from 396 K to 371 K.[38] The controversial results reported by different groups on the solubility ranges for BaO and TiO_2 as well as on the influence of stoichiometry on T_C point towards the existence of metastable states in BTO ceramics depending on the synthesis method.[37] These ambiguities observed for bulk materials could be enhanced on the nanoscale due to changes in the solubility limits depending on surface energies[39] and the aforementioned scaling effects. In this respect, the atomic layer deposition (ALD) technique is predestinated for the exploration of stoichiometry effects in multinary oxides, as the low growth temperatures typically result in an amorphous film, which is crystallized in a subsequent annealing step.[40-42] The required solid-solid transformation should be prone to the formation of metastable, nanocrystalline phases, which can exhibit substantially larger solubility ranges compared to the thermodynamic equilibrium. This was already demonstrated recently, where ALD was employed to produce ~50 nm thick nanocrystalline BTO films on Si/Pt substrates with varying Ba/Ti-ratios ranging from 0.80 to 1.06. These films exhibit no evidence of impurity phases and display a strong dependence of the magnitude of the permittivity to the film composition. The observed change in properties was explained by the formation of Schottky defects for the non-stoichiometric compositions.[42]

In the present paper, we utilize this extended solubility range for BTO thin films based on Schottky defects to control T_C. The manipulation of the Ba/Ti-ratio allows the tuning of T_C in a wide temperature range of 138 K, not only reducing T_C on the Ti-rich side, but also increasing T_C compared to the stoichiometric film on the Ba-rich side. This mechanism is also strain-mediated, but until now was not considered as a way to shift T_C in ferroelectric perovskites. Our temperature dependent study is based on two complementary methods: dielectric measurements and Raman scattering experiments. As the contribution of the grain sizes is accounted for separately, it becomes apparent that the major influence for the shift in T_C arises from the compositional change. In addition, we illustrate how the presence of the hexagonal polymorph in addition to the perovskite phase influences the structural transformation in the thin film on the Ba-rich side.

Experimental

Atomic layer depositions of semi-amorphous $Ba(OH)_2$-TiO_2 laminates of ~50 nm total film thickness on Pt(111)/Ti/SiO_2/Si(100) substrates (Gmek Inc.) were conducted in a Picosun R200 Advanced Reactor. The cation-precursors were Absolut Ba (Air Liquide, $Ba(iPr_3Cp)_2$), kept at 473 K, and titanium-isopropoxide (Alfa Aesar, $Ti(iOPr)_4$), kept at 388 K. For both of them H_2O, kept at room temperature, served as reactant. High purity N_2 gas (99.9999 %) was used as carrier gas and the growth temperature was 563 K. The pulse and purge times were 1.6/6 s for $Ba(iPr_3Cp)_2$ and 0.1/10 s for H_2O for the Ba-O subcycle, and 0.3/1 s for $Ti(iOPr)_4$ and 1/3 s for H_2O for the Ti-O subcycle. An initial 12 Å thick layer of TiO_2 was deposited on all substrates to improve uniformity. In order to vary the overall composition of the films, the repeat number for the Ba-subcycle was kept constant, while the repeat number for the Ti-subcycle was varied between 42 and 55. A sequence of 10 total repeat units of alternating subcycles, as described previously, resulted in a total film thickness of ~ 50 nm.[42]

Metal-insulator-metal (MIM) capacitors were produced by depositing ~80 nm thick 90 x 90 μm^2 squares of Pt before or after (for one stoichiometric sample) annealing, utilizing photolithography and sputtering at room temperature. *Ex-situ* annealing under an over-pressure of 5 psi O_2 was conducted using the following annealing sequence: the samples were heated to 1023 K with a rate of 4 $K \cdot min^{-1}$, kept at 1023 K for 12 hours, cooled to 353 K at a rate of 1 $K \cdot min^{-1}$. A subsequent step with heating to 433 K (3 $K \cdot min^{-1}$) followed by cooling to 373 K at a slow rate of 0.5 $K \cdot min^{-1}$ was applied to ensure a slow cooling through the Curie temperature of bulk $BaTiO_3$ (T_C=396 K).[43]

The grazing incidence X-ray diffraction (GI-XRD) scans were performed on a Rigaku Smartlab using Cu-K_α radiation. The lattice parameters were extracted from least squares fits utilizing the WinCSD program package.[44]

Cross-sections of the MIM-capacitors for high resolution transmission electron microscopy (HR-TEM) were prepared in a Helios Nanolab 600i (FEI, USA) Scanning Electron Microscope (SEM)/Focused Ion Beam (FIB) dual beam system equipped with gas injectors for W and Pt deposition and an Omniprobe micromanipulator (Omniprobe, USA). After depositing a 2 µm thick protective Pt layer, milling using a 30 keV Ga^+ ion beam resulted in a cross-section area of 5 × 5 μm^2, which was subsequently polished

with 5 keV and 2 keV Ga^+ ion beams, respectively. These MIM-cross sections were investigated utilizing a Titan 80–300 operated at 300 kV, which is equipped with a high-angle annular dark-field (HAADF) detector (Fischione, USA), a spherical aberration (C_s) probe corrector and a post-column Gatan image filter (GIF). Digital Micrograph (Gatan, USA) and Tecnai Imaging and Analysis (FEI, USA) software were used for the image processing.

X-ray photoelectron spectroscopy (XPS) measurements were conducted using a Physical Electronics VersaProbe 5000 under a base-pressure of ~10^{-6} Pa. An Al-Kα source provided incident photons with an energy of 1486.6 eV at 10 kW mm^{-2}. The XPS spectra were collected with the pass energy of 23 eV. An electron neutralizer was used to neutralize the surface. Linear energy correction was applied in reference to the carbon spectra. The energy of the C1s peak of non-oxidized carbon was set at 284.8 eV. The detector was placed at the angle of 87.2° relative to the surface in order to collect the XPS signal from a larger volume of the films.

The electrical properties of the MIM-capacitors were measured in a probe station (Lakeshore Cryotronics TTP4) utilizing a Keithley SCS-4200 electrometer for collecting frequency dependences (10kHz - 1MHz) of capacitance & loss tangent and a Precision Tester (Radiant Technologies, Inc.) for collecting polarization hysteresis loops. The measurements were performed in air at room temperature and under vacuum of ~10^{-5} Torr over a temperature range of 190–420 K, on cooling and heating, at a constant rate of 5 K min^{-1}.

Raman spectra were collected in backscattering configuration $z(x, x+y)\bar{z}$ using a single monochromator (XploRA, Horiba Jobin-Yvon, Edison, NJ) and a laser (4 mW, λ = 532 nm) focused to a spot diameter of ≈10 µm at an intensity of 1.6×10^3 W cm^{-2}. Light was dispersed using a 2400 gr mm^{-1} grating and collected using a Peltier-cooled array detector. The sample temperature was varied from 123 K to 473 K (Linkham THMS 600, instrumental precision ±0.1 K) in increments of 5 K at a heating ramp rate of 5 K min^{-1}. The sample is also allowed to equilibrate for 1 min between consecutive Raman scans.

Results & discussion

Material characterization.

Four BTO thin films with varying Ba/Ti ratio were grown by ALD and were characterized by XRD, RBS, TEM, XPS, and Raman scattering techniques. Details on the structural characteristics of the samples are provided elsewhere.[42]

Room-temperature X-ray diffraction scans, collected after the annealing step reveal the presence of polycrystalline BTO in the perovskite structure for all samples and, independent of the composition, no additional peaks are detected. The GI-XRD patterns point towards a cubic symmetry or a marginal tetragonal distortion. However, Raman spectra clearly show the tetragonal symmetry for the perovskite in coexistence with the hexagonal BTO polymorph within all thin film samples. The Ba/Ti-ratio values have been determined using RBS measurements. The details of the RBS analysis are provided elsewhere.[42] **Figure 1** shows the lattice parameters, which were extracted from least squares fits to the cubic perovskite structure (SG: $Pm\bar{3}m$). A lattice expansion of 0.2 % with increasing Ba/Ti-ratio is observed. The mean values and standard deviations of crystallite sizes determined from the Gaussian fittings (Fig. S1) of the distribution of sizes obtained from TEM images are also depicted in Fig. 1. Detailed TEM investigations have been performed for all films, which had top Pt electrodes deposited *before* the annealing procedure. The results of this study (see Ref. 42 for details) imply that an extended metastable solubility range exists for the perovskite-phase on both sides of the stoichiometric composition. The absence of any additional secondary phases besides the hexagonal polymorph, together with the lack of cation segregation at the grain boundaries and film-substrate interfaces confirm that the off-stoichiometry is accommodated within the BTO crystallites. Moreover, the independence of the ratio of hexagonal to perovskite polymorph to the Ba/Ti-ratio and the systematic change of the lattice parameter indicate that cation defects are located in the perovskite phase.[42]

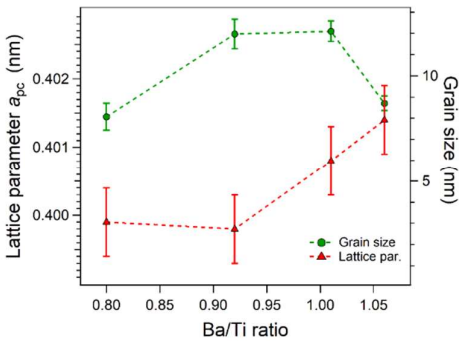

Figure 1. Lattice parameters for the pseudo-cubic structure, a_{pc} (from XRD), and average crystallite size (from TEM) as a function of Ba/Ti ratio.

In the present work, we additionally investigated a stoichiometric (Ba/Ti=1.01) sample by TEM, where the *top electrodes* were deposited *after* the annealing process. A cross section of the MIM-capacitor was examined between the top and bottom Pt electrodes to unravel the influence of the presence/absence of a top electrode during the annealing process on the crystallite size and resulting physical properties. **Figure 2** shows representative BF-TEM images for two stoichiometric (Ba/Ti = 1.01) samples, one with *top electrodes* deposited *before* annealing (Fig. 2a) and the other one with *top electrodes* deposited *after* annealing (Fig. 2b). The distribution of crystallite sizes obtained from the TEM images for each sample and their fitting are presented in Figs. S1 and S2, respectively. As expected, the comparative analysis indicates that the crystallite growth is suppressed by the presence of a top electrode during the annealing process. While the distribution of crystallite sizes is fitted by one Gaussian function with a mean value of 12.1 nm for sample with electrodes *before* annealing, the size distribution is fitted by two Gaussians, with the mean values of 12.0 and 35.0 nm sizes for sample with electrodes *after* annealing. In addition, the cross

section between the free area (no top electrodes) and bottom electrode obtained for a stoichiometric sample was also analysed. The distribution of grain sizes obtained from TEM images of this cross section and the fitting are presented in Fig. S3. For this case, the main value of crystallite size is 17.1 nm. Below we will show how the difference in crystallite size affects the ferroelectric phase transition.

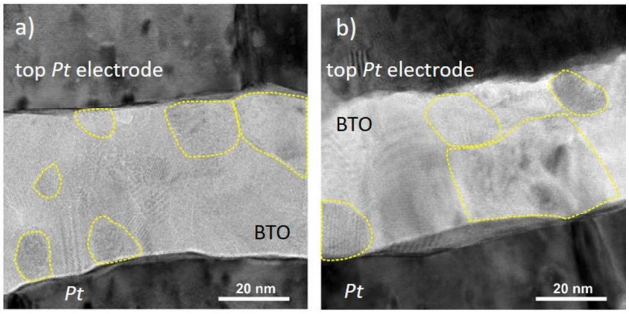

Figure 2. BF-TEM cross sections of the MIM-structures after the annealing step for the thin films with Ba/Ti-ratio of 1.01 with top Pt electrodes deposited a) before and b) after the annealing procedure. The yellow dashed lines highlight some crystallites within the cross sections.

The valence states of Ti and Ba and their possible change with compositional variation have been probed by XPS. The Ti and Ba spectra and their fitting are presented in the Supporting Information. Figure S4 unambiguously demonstrates that Ti in the oxidation state 4+ is present in all films independent of composition. The XPS Ba spectra collected for the films with various Ba/Ti ratios, displayed in Figure S5, show that the Ba3d5/2 peak contains two lines, corresponding to the Ba^{2+} ions located in deeper layers of the films and on the surface with a shift to higher energy. The intensity of the line originating from the Ba^{2+} ions from the bulk of the films monotonically increases, while the intensity of the line corresponding to the Ba^{2+} on the surface systematically decreases with increasing Ba/Ti ratio. We note that independent of the composition no recharging effects of the cations is observed.

Dielectric study.

Frequency dependences (from 10 kHz to 1 MHz) of the capacitance and loss tangent were collected within temperature intervals of 190 K<T<420 K for the films with Ba/Ti ratios of 0.8, 0.92 and 1.01, and between 250 K and 420 K for the film with a Ba/Ti ratio of 1.06. First, the samples were cooled down from room temperature to 190 K/250 K, followed by heating up to 420 K and a subsequent cooling to room temperature. A negligible frequency dependence of the permittivity and loss tangent was observed within the investigated temperature intervals for all samples. Representative temperature dependent data obtained at 100 kHz for four samples with the *top Pt electrodes* deposited *before* the annealing procedure are depicted in **Figure 3**. In all cases, the dielectric constant is normalized to its maximum value ε_m. The absolute maxima of the dielectric constant and temperature extracted from the cooling and heating cycle are summarized in **Table 1**. As displayed in **Fig. 3a**, the samples exhibit a broad non-monotonic dependence with hysteretic behaviour. The maximum permittivity shifts from 212 K to 350 K for cooling and from 230 K to 355 K for heating as the Ba/Ti ratio increases from 0.8 to 1.06, respectively. The temperature dependence of the dielectric loss (tanδ) reveals a distinctly different behaviour for each composition (**Fig. 3b**). While a broad, but at the same time, rather pronounced maximum around 200 K for a Ba/Ti ratio of 0.8 is present, this maximum becomes smoother with increasing Ba-content and practically vanishes at the stoichiometric composition. However, in the Ba-rich sample the scenario is vastly different as the loss tangent not only increases with temperature, but is in general higher than for all other samples. This behaviour might indicate the segregation of space charges at grain boundaries. Considering the formation of Schottky defects as the main source for off-stoichiometry, the amount of oxygen vacancies is higher in Ba-rich than in Ti-rich sample (see equations (2) and (3) below), so space charges might form more readily in this case. To further consider the influence of the leakage current on the temperature behavior of losses, we provide the electric field dependences of current density (J-E) for the films with different Ba/Ti-ratio. The dependences depicted in Fig. S6a demonstrate that the films with different stoichiometry are basically identical in their J-E response, so there is no correlation between the J-E behavior and features in Fig. 3b for the film with Ba/Ti=1.06.

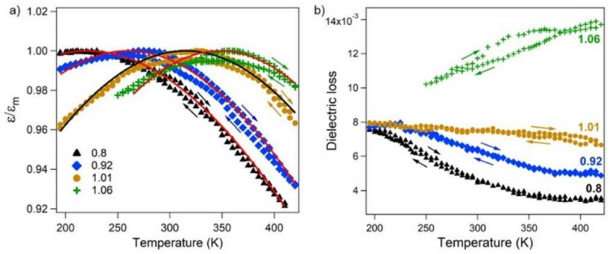

Figure 3. Temperature dependence (cooling and heating cycles) of a) normalized dielectric constant and b) dielectric loss as a function of the Ba/Ti ratio. Markers – experimental data, lines – fits to equation (1) for the heating cycle.

The maximum in ε(T) is indicative of a phase transition in ferroelectric materials. The total shift of the peak temperature T_m over the studied frequency range cannot be clearly determined because of its broad occurrence. Nevertheless, it is worth mentioning that the weak frequency dispersion of T_m should still be present due to the diffuse type of the transition as we will elaborate below. Since ε(T) exhibits thermal hysteresis, a first-order ferroelectric phase transition should be present, which is similar to bulk BTO. A progressive reduction of the hysteresis with increasing Ba/Ti ratio is observed. The hysteresis exhibits the largest value of 18 K for the most Ti-rich sample (Ba/Ti = 0.8), continuously decreases to 10 K for the nearly stoichiometric sample (Ba/Ti = 1.01) and ultimately shrinks to 5 K for the most Ba-rich sample.

Compared to the single-crystal counterparts and larger grain ceramic specimens with stoichiometric composition, the transition temperature drops dramatically. This decrease of T_C definitely relates to the reduced crystallite sizes, as analogous shifts in the ferroelectric transition temperature were observed in a number of ceramic and thin film samples: e. g., the T_C was registered at 379 K for 50-nm[45] and 30-nm[37] ceramic samples and at 333 K for grain sizes of 22 nm[46]. In analogy, the decrease of the Curie temperature was reported for polycrystalline BTO films as a function of the film thickness and grain size.[47]

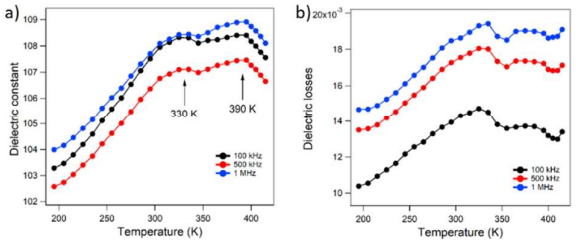

Figure 4. Temperature dependences (on heating) of a) dielectric constant and b) losses at three representative measuring frequencies for the stoichiometric sample (Ba/Ti= 1.01) with *top electrodes* deposited *after* the annealing step. Markers are experimental data; lines are guides to the eye.

To probe how the crystallite size affects the temperature behaviour of dielectric parameters for the present thin films, and thereby disentangle the size effect from a compositional effect, we also investigated the stoichiometric (Ba/Ti = 1.01) sample with the *top electrodes* deposited *after* the annealing step. In this case, the crystallites underneath the top electrodes are larger and the distribution of grain sizes is different from the sample, in which the top electrodes were deposited before the annealing procedure (see Figs. S1c and S2). This difference clearly shows that an additional layer on top of the thin film effectively reduces the grain growth compared to an unconfined film surface. **Figure 4** reveals the presence of two peaks in ε(T) and tanδ(T) dependences for the MIM-capacitor with the *top electrodes* deposited *after* the annealing step. The first peak is observed around T_m = 330 K and the second one at T_m = 390 K. The dependences can be considered as frequency independent, although they exhibit a very broad transition region and, therefore, a diffuse type phase transition. A comparison between the grain size distributions for the samples with top electrodes *before* and *after* annealing allows us to attribute these maxima to the phase transitions for crystallites of two groups, with smaller (average 12 nm) and bigger (average 35 nm) sizes. The bigger grains are also clearly visible in the TEM image displayed in Fig.2b and the wide grain size distribution results in the very broad phase transition region displayed in Fig. 4. It should be noted that the peak at higher temperature (T_m = 390 K) is very close to the Curie temperature for bulk samples (T_C = 396 K)[43], and the peak at lower temperature (T_m = 330 K) can be associated with a decreased T_C due to the crystallite size reduction and is very close to T_m = 315-325 K for the sample with *top electrodes* deposited *before* the annealing step. This comparison allows us to independently discern the crystallite size effect and hereby confirm that the change of the transition temperature observed for the samples with different Ba/Ti ratio (see Fig.3a and Table 1) is predominantly caused by the different compositions. Thus, we reveal a huge shift in the transition temperature of ΔT = 138 K due to the variation in the cation ratio from 0.8 to 1.06. Taking into account similar fabrication conditions, film thicknesses, and grain sizes (see Fig.1) for all four samples, it becomes apparent that the dramatic deviation of the transition temperature is directly correlated to the variation of stoichiometry. Such a big increase of the Curie point, ΔT = 120 K, due to variation of the Li/Nb ratio from 0.96 to 1.04, has been observed earlier in $LiNbO_3$ crystals.[48] A smaller increase of T_C, about 10 K, due to variation of Ba/Ti ratio from 0.99 to 0.999 has been demonstrated in ceramic BTO samples.[37] Compared to BST ceramics, this large shift in Curie temperature corresponds to a change in the Ba/Sr-ratio of more than 50%. Before discussing which microscopic mechanisms could provoke this effect, we shall first analyse the behaviour of the dielectric constant.

Table 1. Maximum temperature, T_m, and dielectric constant, ε_m, extracted from experimental temperature dependence for the four films with top electrodes deposited *before* annealing. Parameters Δ and ξ from least square fits to equation (1)

Ba/Ti ratio	T_m on cooling/heating (K)	ε_m on cooling/heating	Δ (K)	ξ
0.8	212 / 230	84.6 / 84.6	650 ± 6	2
0.92	258 / 275	110.7 / 110.9	593 ± 5	2
1.01	315 / 325	168.6 / 169.3	588 ± 6	2
1.06	350 / 355	163 / 163.8	565 ± 10	2

The decrease of T_C because of grain size reduction is typically accompanied by the broadening of the maximum and decreasing of the dielectric constant. **Table 1** shows how the maximum dielectric constant, ε_m, changes with composition variation. The room temperature dielectric constant as a function of frequency for the films with Ba/Ti=0.8, 0.92, 1.01 and for the film with Ba/Ti=1.01 with *top electrodes after* annealing is depicted in Fig. S6b. As was mentioned in our prior paper, the room temperature dielectric constant strongly depends on stoichiometry, especially on the Ti-rich side. It is reduced by 50% in the Ti-rich samples compared to the stoichiometric one, but remains almost unchanged upon further increasing the Ba/Ti ratio.[42] In the present work, the same trend is observed for ε_m from the temperature dependence of the dielectric constant. As noted above, the phase transition in fine grained samples is very broad and is therefore coined a diffuse phase transition (DPT). A simple and explicit model qualitatively and quantitatively describing the temperature dependence of the dielectric permittivity at the DPT was suggested:[49]

$$\varepsilon = \frac{\varepsilon_m}{1+((T-T_m)/\Delta)^{\xi}} \qquad (1)$$

where Δ and ξ are empirical parameters related to the transition diffuseness and to the character of the phase transition, respectively. The parameter Δ is the peak broadening that indicates the degree of diffuseness. The parameter ξ can take values between 1 for a typical ferroelectric behaviour and 2 for the so-called "complete" DPT. The solid curves depicted in Fig.3a are fitting

results to equation 1. All data are best fitted with a parameter ξ=2 and the parameters Δ shown in **Table 1**. A slight, gradual decrease of the diffuseness degree with increasing Ba/Ti ratio can be noticed.

Due to the wide distribution of grain sizes, there is a range for the T_C in a DPT, so the peak temperature T_m can be regarded as an average T_C (correlated to the average grain size). Keeping this in mind, we use the term *phase transition temperature* for the *peak temperature* T_m in the discussion below.

Accounting average grain sizes of 8-12 nm in all compositions (see Fig.1), we approach the ferroelectricity limit. Indeed, **Figure 5a** shows an extremely narrow hysteresis loop collected at 300 K at 500 Hz. We observe here that the polarization changes as a function of Ba/Ti ratio in a similar manner as the dielectric constant (see Table 1). The values of both, maximum polarization P_{max} (at E = 0.545 MV/cm) and remnant polarization P_{rem} drop by almost 50% for the Ti-rich samples and only slightly decrease in the Ba-rich sample compared to the stoichiometric one. **Figure 5b** presents the temperature behaviour (heating cycle) of the values of maximum and remnant polarization as a function of Ba/Ti ratio. While P_{max} remains almost unchanged over the phase transition region for all compositions, P_{rem} exhibits a non-monotonic behaviour with a weak and wide hillock around T_m for the Ti-rich films (Ba/Ti = 0.8, 0.92) and with more pronounced and narrower maxima for the stoichiometric and the Ba-rich (Ba/Ti=1.06) samples. Considering practically similar grain sizes for all compositions, such a difference indicates that the latter two films contain more crystallites with stable domains or domain structure, which contribute to the polarization in zero electric field. These crystallites are likely more strained and therefore should have a higher ratio of tetragonality (c/a) or lower symmetry. Furthermore, the remnant polarization, although approaching zero at elevated temperature, does not vanish above T_m for these two samples, implying that there are residual strains in the vicinity of the DPT on the high-temperature side that preserve the polarization within the grains. For Ti-rich samples, the remnant polarization remains almost zero over the entire temperature region. Therefore, the samples are expected to have more strain relaxed crystallites with minor or no distortion from cubic symmetry (c/a->1). The room-temperature hysteresis loop for the stoichiometric sample with *top electrodes* deposited *after* the annealing step is displayed in **Figure 6**. While the maximum polarization for this film is similar, the remnant polarization is enhanced by a factor of 3 compared with the same sample with *top electrodes* deposited *before* annealing (Fig. 5). This difference most certainly arises from the presence of larger crystallites within this thin film.

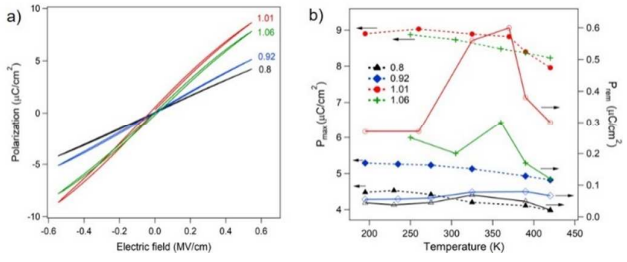

Figure 5. Polarization behaviour: a) hysteresis loops at 305 K and b) temperature dependence (on heating) of maximum polarization P_{max} at E=0.545 MV/cm (left) and remnant polarization P_{rem} at E=0 (right) for samples with various Ba/Ti ratio. The dashed and solid lines are guides for eye.

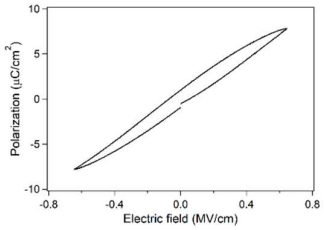

Figure 6. Room-temperature hysteresis loop collected at 1 kHz for the thin film with Ba/Ti-ratio of 1.01 and *top electrodes* deposited *after* the annealing step.

From a microscopic point of view, the shift of the ferroelectric transition temperature in BTO is a strain/stress mediated phenomenon for any kind of effect (including any interfacial and gradient effects). We would like to underscore that in contrary to epitaxial films, the strain due to the lattice mismatch between substrate and film has a negligible influence on the structure of polycrystalline BTO films. As TEM images show (see Fig.2), the crystallites within all films are randomly oriented, so no preferential alignment occurs. This fact is further corroborated by XRD data, which show the polycrystalline nature of all thin films.[42] Moreover, as the growth and annealing conditions were kept identical for all samples, we assume that the strain induced by the thermal expansion mismatch between substrate and film is equivalent for all films. With respect to the compositional gradient effect, we refer again to the microstructure analysis and further note that no measurable cation segregation at the grain boundaries is observed from TEM.[42] Therefore, we focus on the impact of the composition hereafter.

For compositional effects within the lattice the strain arises from the defects formed during the crystallization of BTO, so called *Vegard strain* (or chemical pressure).

In off-stoichiometric BTO the following types of partial Schottky defects are typically considered[50,51]

Ti-rich side: $TiO_2 \xrightarrow{BaTiO_3} Ti_{Ti}^{X} + 2O_O^X + V_{Ba}'' + V_O^{\bullet\bullet}$ (2)

Ba-rich side: $BaO \xrightarrow{BaTiO_3} Ba_{Ba}^{X} + O_O^X + V_{Ti}'''' + 2V_O^{\bullet\bullet}$ (3)

Now we estimate the strain due to the presence of partial Schottky defects, with respect to stoichiometric deviations in the chemical formula. For this purpose, we use the results of calculations made by Freedman *et al.* for strontium titanate (STO).[52] Since BTO is very similar to STO in terms of chemical bonding, the perovskite crystal structure, and lattice parameters, the estimation of the chemical strain in BTO using these results seems appropriate. The local strains imposed by different defects such as oxygen vacancies (V_O), strontium vacancies (V_{Sr}), titanium vacancies (V_{Ti}), strontium-oxygen divacancies (V_{Sr}-V_O), and titanium-oxygen divacancies (V_{Ti}-V_O) determined in Ref. 52 are provided in **Table 2**. Here, ε_c is the chemical strain ($\Delta a/a$), and δ denotes the deviation from stoichiometry that specifies the number of defects per

chemical unit. Positive Vegard strain results in lattice expansion, and negative Vegard strain in lattice contraction.

Table 2. The ratio of the chemical strain to stoichiometric defect deviation δ for $Sr_1TiO_{3-\delta}$, $Sr_{1-\delta}TiO_3$, $SrTi_{1-\delta}O_3$, $Sr_{1-\delta}TiO_{3-\delta}$, and $SrTi_{1-\delta}O_{3-\delta}$ (taken from Ref. 52)

	V_O	V_{Sr}	V_{Ti}	V_{Sr}-V_O	V_{Ti}-V_O
ε_c/δ	+0.001	+0.030	+0.402	-0.008	+0.260

Our Ti-rich samples can be treated as $Ba_{1-\delta}TiO_{3-\delta}$, while Ba-rich samples as $BaTi_{1-\delta}O_{3-2\delta}$ in accordance with equations (2) and (3), respectively. First we estimate the contribution of the partial Schottky defects to the strain. For this, we calculated the strain ε_c which should be created if a) only isolated vacancies are introduced, and b) if only divacancies (and additional V_O for Ti-deficient films to maintain charge balance) are introduced. For the stoichiometric composition ($\delta = 0$) we assume an unstrained state ($\varepsilon_c = 0$). The calculated strain versus Ba/Ti ratio is displayed in **Figure 7**. The strain determined using the lattice parameters from XRD data (see Fig.1) is also depicted in Fig. 7. A pseudo-cubic lattice parameter for stoichiometric BTO, a_{pc}=4.007 Å (this is an average value for the tetragonal structure, where a=3.992 Å and c=4.036 Å) was used. In addition, the variation of the phase transition temperature (bars indicate the T_m values on cooling and heating taken from Table 1) as a function of the Ba/Ti ratio is presented in Fig. 7. The dependence for T_m follows a linear relation as indicated by a least-squares fit. Comparison of the estimated values of the strain with experimental values allows us to conclude that the strain produced by divacancies exhibits a similar trend as the experimentally observed strain with negative strain on the Ti-rich side and positive strain on the Ba-rich side. However, the strain obtained using lattice parameters from XRD is smaller than the theoretically predicted strain arising from partial Schottky defects. For possible sources of strain relaxation, the following contributions could be considered: with respect to the internal stress at the grain boundaries, different mechanisms of its evolution were suggested, and there is not a consensus so far. Although many calculations show that the driving force for the internal tensile stress is surface energy reduction due to grain boundary formation,[53] the measured value of this stress is much lower than that attributed to compressive stress due to insertion of additional atoms into the grain boundaries as a way to relax the tensile stress in the film.[53,54] We do not observe any segregation of cations at the boundaries from TEM, and therefore assume that quite high internal tensile stress is present in our samples. This suggestion is supported by the fact, that several polymorphs (cubic, tetragonal and hexagonal) are formed for all compositions due to the non-equilibrium state. This internal stress at the grain boundaries could facilitate the relaxation of the strain due to partial Schottky defects located inside crystallites. Regarding the second possible source, we observe compositional inhomogeneity from elemental mapping in TEM cross sections.[42] This spatial off-stoichiometry likely occurs in order to lower the total energy and therefore might also relax the local strain induced by Schottky defects.

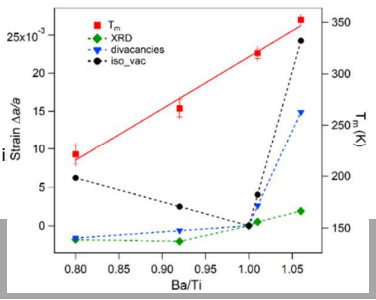

Figure 7. Strain from theoretical calculations (circles, triangles), strain determined from XRD (diamonds) and transition temperature T_m (squares) versus Ba/Ti ratio. Markers are experimental or calculated values, solid line is a linear fit (y=-188 + 505x), dashed lines are for clarity.

Raman scattering study.

To complement and support our dielectric study, we conducted a detailed analysis of the Raman spectra collected in the temperature range from 123 K to 473 K (heating cycle) for the two thin films with lowest and highest Ba/Ti-ratio, 0.8 and 1.06, respectively. All spectra were collected in areas of the film surface between the top Pt electrodes. It should be mentioned that the Raman spectra for samples with *top electrodes* deposited *before* and *after* annealing are similar, which means that the microstructure between the top electrodes is basically identical independent of the top electrodes deposition procedure. **Figure 8** shows the room-temperature spectrum collected for the stoichiometric (Ba/Ti=1.01) sample which has top electrodes deposited before annealing. The spectrum demonstrates the presence of tetragonal (*t*-BTO) and hexagonal (*h*-BTO) polymorphs and is representative for all thin films used in this study.[42] No peaks from impurity phases are visible. Note that a polymorphous mixture is frequently observed for polycrystalline BTO thin films and was also reported for nanoparticles with a size of 40 nm.[55-57]

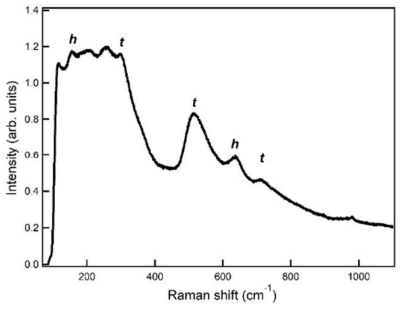

Figure 8. Room-temperature Raman spectra for the stoichiometric thin film (Ba/Ti=1.01) with top electrodes before annealing.

The temperature dependent Raman spectra collected for the samples with Ba/Ti-ratios of 0.8 and 1.06 qualitatively look similar to the room-temperature spectra displayed in Figure 8. The wide band in the wavenumber range of 150-300 cm^{-1} contains several overlapped modes including the ~180 cm^{-1} peak assigned to the E_{2g} mode of *h*-BTO[58] and the ~280 cm^{-1} peak assigned to the $A_1(TO_2)$ mode of *t*-BTO.[59] However, each of these peaks is not well isolated and has contributions of a few modes. Therefore, it is impossible to use these peaks for a meaningful analysis. The 520 cm^{-1} peak primarily represents the $A_1(TO_3)$ component of the $A_1(TO)$ spectrum of *t*-BTO.[59] As was shown recently, the frequency of the 520 cm^{-1} mode of *t*-BTO gradually decreases and its width broadens until the

mode almost disappears above the ferroelectric transition in a polycrystalline BTO thin film.[60] For the hexagonal polymorph a very prominent ~620 cm^{-1} peak is assigned to the A_{1g} mode.[58] As seen in Fig.8, the Raman spectra also contain a ~720 cm^{-1} peak, which represents the $A_1(LO_3)$ mode of *t*-BTO.[59] This peak is broad and has a low intensity. Moreover, its frequency remains practically constant throughout the tetragonal phase.[59] According to different studies, the soft mode in the perovskite BTO has two components: a doubly degenerate overdamped component $E(TO_1)$, the frequency of which varies within 35±5 cm^{-1}, and the half-width is 85–115 cm^{-1} and the totally symmetric component $A_1(TO_2)$ at a frequency of 280-308 cm^{-1}.[59,60] While the overdamped component $E(TO_1)$ condenses very fast and becomes invisible approaching the ferroelectric phase transition, the frequency of the $A_1(TO_2)$ component remains almost unchanged with temperature in polycrystalline thin films.[60] In our Raman spectra, the situation is more complicated due to the presence of a polymorphous mixture in all samples. When a soft mode is overdamped or even unavailable in a material with structural disorder, it is appropriate to obtain information about the phase transformation by monitoring the temperature behaviour of the spectroscopic parameters of other modes, which are sensitive to the symmetry of the structure.[16,61] Considering all these factors, we decided to base our analysis on separately evaluating the temperature behaviour of the frequency, integrated intensity, and FWHM (full width at half maximum) for the 520 cm^{-1} (*t*-BTO) and 620 cm^{-1} (*h*-BTO) peaks. Bose-Einstein correction has been performed prior to the data analysis of structural phase transitions; in addition, fitting with a Lorentzian lineshape has been applied following the methodology described in detail previously.[62]

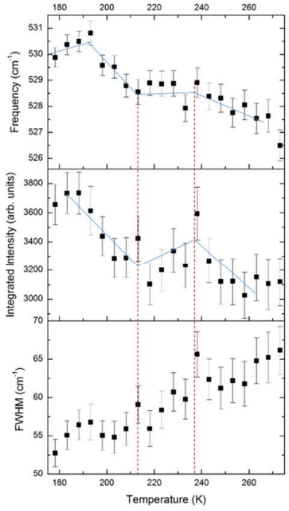

Figure 9. Temperature dependences of the frequency, integrated intensity and FWHM of the 520cm^{-1} peak for the Ti-rich sample (Ba/Ti=0.8).

Figure 9 shows the temperature dependences of the spectroscopic parameters of the 520 cm^{-1} peak for the Ti-rich sample (Ba/Ti=0.8). As demonstrated, the frequency of the 520 cm^{-1} peak decreases non-monotonically from 532 cm^{-1} to 526 cm^{-1} as the temperature increases from 100 K to 320 K. The reduction rate sharply changes at ~212 K. Starting from this point, the frequency remains unchanged until ~230 K and continues to gradually decrease above 230 K. The integrated intensity displays an anomaly in the same temperature range, while the FWHM consistently increases over the entire temperature interval. All the features occur in the same temperature interval as the phase transition observed in dielectric measurements for this film. The temperature behaviour of the 620 cm^{-1} peak is not so distinct (see Fig.S9). Its frequency continuously increases and a slight change in the slope can be noticed in the interval from 212 K to 230 K. Other parameters, i.e. the width and integrated intensity, change marginally and monotonically, with no specific features detectable between 212 K and 230 K. Based on this analysis we conclude that the phase transition around 212-230 K revealed in the dielectric study is fully attributed to the structural transformation of the perovskite phase from tetragonal to cubic with increasing temperature, although the symmetry change marginally influences the dynamics of the *h*-BTO phase. Moreover, the extended temperature interval for this specific behaviour of the spectroscopic parameters for the 520 cm^{-1} mode, confirms the diffuseness of the phase transition.

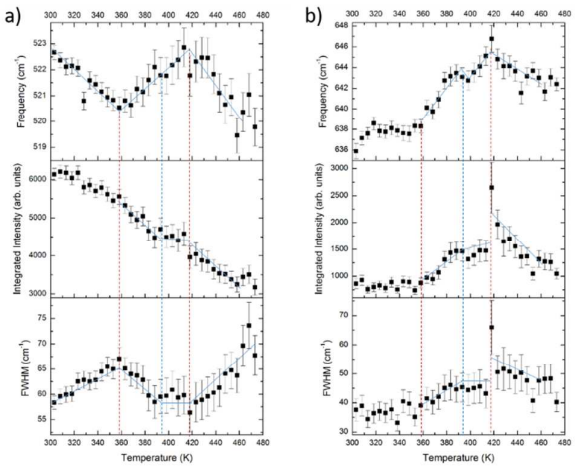

Figure 10. Temperature dependences of frequency, integrated intensity and FWHM of the 520 cm^{-1} (a) and 620 cm^{-1} (b) peaks for the Ba-rich sample (Ba/Ti=1.06).

Figure 10 displays the frequency, integrated intensity and FWHM as a function of temperature for the 520 cm^{-1} and the 620 cm^{-1} peaks for the most Ba-rich thin film (Ba/Ti=1.06). Here, a significant change in the frequency behavior of the 520 cm^{-1} peak is observed over a wide temperature interval, from 350 K to 415 K. While the frequency decreases as temperature increases from 290 K to 350 K, it starts to raise at 350 K followed by a sharp drop at 415 K. The integral intensity and linewidth also experience non-monotonic changes in the same temperature range. While the decrease in the intensity slows down at 350 K and only drops a little between 350 K and 415

K, the FWHM sharply changes the behaviour, from increasing to decreasing, at 350 K and then changes the behaviour again, now from decreasing to increasing, at 415 K. The temperature behaviour of the 620 cm^{-1} peak for the Ba-rich sample exhibits a behaviour strongly correlated to the 520 cm^{-1} peak and even exhibits additional features. As we can see, all parameters have significant peculiarities in the interval of 350 – 420 K. An additional anomaly occurs within this range, at ~400 K. This feature is observed for all spectroscopic parameters of the 620 cm^{-1} peak. Analysis of both peaks for the Ba-rich sample indicates that the structural transformation of both phases, *t*-BTO and *h*-BTO, occurs simultaneously and/or facilitates each other. The observation of the phase transition in the Raman study for the sample with a Ba/Ti-ratio of 1.06 allows a deeper insight into the nature of the structure transformation. Although the phase transition region observed in the Raman spectra includes the transition temperature obtained in dielectric measurements at 350 K to 355 K, the Raman study indicates that the transformation has an extended character and covers a wider temperature range up to 420 K. There are two reasons, which could cause such a difference: the sample location, at which the Raman spectra were collected (area between top electrodes) might have bigger crystallites in addition to the smaller ones below the electrodes, which are probed in dielectric measurements or the higher losses, which are detected in this sample, could mask additional features that occur during the phase transition for the dielectric measurements. This concerted phase transition of both polymorphs could account for the unprecedented increase of the Curie temperature compared to the stoichiometric composition.

Conclusions

In summary, we show a novel route to manipulate a ferroelectric phase transition in nanograined ferroelectric thin films. The presented approach is based on the enhanced metastable cation solubility in nanograined polycrystalline BTO thin films, which results in the formation of Schottky defects. Measurements of the temperature dependence of the dielectric constant reveal that the transition temperature changes linearly from 212 K to 350 K as the Ba/Ti ratio increases from 0.8 to 1.06 for films with average grain sizes of 8-12 nm. A significant reduction in the temperature dependence of the dielectric permittivity that can be desired for some practical applications is observed and arises from a completely diffuse phase transition for all compositions. However, the degree of diffuseness slightly decreases from ~650 for a Ba/Ti-ratio of 0.8 sample to ~565 for 1.06. For two nearly stoichiometric films (Ba/Ti=1.01) with different processing sequences, a size effect manifests itself in the decrease of the Curie point from 390 K for crystallites with average size of 35 nm to 330 K for crystallites with average size of 12 nm. This allows to disentangle the contribution of the size effect to the transition temperature change from compositional effects. We propose that partial Schottky defects forming mostly divacancies (V_{Ba}-V_O, V_{Ti}-V_O) are created to accommodate the off-stoichiometry. However, the estimates show that internally imposed strain via chemical pressure should be higher than that registered by XRD. Therefore, the internal stress evolving at the grain boundaries during the crystallization process of the thin films in conjunction with a locally varying composition throughout the film are suggested to partially relax the local strain induced by Schottky defects inside the crystallites.

Temperature dependent Raman experiments confirm the transition temperature obtained from dielectric measurements. Monitoring the temperature behaviour of different modes corresponding to the hexagonal and perovskite BTO phases reveals that the presence of the hexagonal polymorph in addition to the perovskite phase influences the structural transformation on the Ba-rich side, while it is ineffective on the Ti-rich side. For the Ba-rich thin film, the Raman study indicates that although the phase transition region includes the transition temperature of 350 K determined from the dielectric measurements, structural reconstructions exhibit an extended character and occur over a wider temperature range up to 420 K.

Conflicts of interest

There are no conflicts to declare.

Acknowledgements

Work at Drexel University was supported primarily by the Office of Naval Research under grant no. N00014-15-11-2170. A.J.R. and A.G.-P. were supported by NSF DMR 1608887. The experiments were partially conducted using the equipment of the Resource Center of Probe and Electron Microscopy (Kurchatov Complex of NBICS-Technologies, NRC “Kurchatov Institute”). We acknowledge the Centralized Research Facilities at Drexel University for access to XRD (NSF DMR 1040166) and XPS (NSF CBET 0959361).

References

1 B. H. Park, B. S. Kang, S. D. Bu, T. W. Noh, J. Lee and W. Jo, *Nature*, 1999, **401**, 682-684.
2 M. Pešic, C. Künneth, M. Hoffmann, H. Mulaosmanovic, S. Müller, E. T. Breyer, U. Schroeder, A. Kersch, T. Mikolajick and S. Slesazeck, *J. Comput. Electron.*, 2017, **16**, 1236–1256.
3 A. Karalis, J.D. Joannopoulos and M. Soljacic, *Annals of Physics*, 2008, **323**, 34–48.
4 M. Song, P. Belov and P. Kapitanova, *Appl. Phys. Lett*., 2016, **109**, 223902.
5 A. Ahmed, I. A. Goldthorpe and A. K. Khandani, *Appl. Phys. Rev*., 2015, **2**, 011302.
6 S. R. Johnston, Y. Yang, Y.-T. E. Cui, Y. Ma, T. Kampfe, L. M. Eng, J. Zhou, Y.-F. Chen, M. Lu and Z.-X. Shen, *J. Appl. Phys.*, 2017, **122**, 074101.
7 V. V. Lemanov, E. P. Smirnova, P. P. Syrnikov and E. A. Tarakanov, *Phys. Rev. B*, 1996, **54**, 3151.
8 V. B. Shirokov, V. I. Torgashev, A. A. Bakirov and V. V. Lemanov, *Phys. Rev. B*, 2006, **73**, 104116.
9 B. Jaffe, W.R. Cook and H. Jaffe, *Piezoelectric Ceramics* Academic Press: London, 1971.
10 I. A. Kornev, L. Bellaiche, P.-E. Janolin, B. Dkhil and E. Suard, *Phys. Rev. Lett*., 2006, **97**, 157601.

11 S. Triebwasser, *Phys. Rev*., 1959, **114**, 63-70.
12 H. Zhang, B. Liu, C. Zhang, C. Qiu, X. Wang, Y. Zhang, X. Lv, L. Wei and Q. Li, *Chem. Phys. Letters*, 2018, **699**, 80–84.
13 P. Perriat, J. C. Niepce and G. Caboche, *J. Therm. Anal. Calorim*., 1994, **41**, 635-649.
14 A. N. Morozovska, M. D. Glinchuk and E. A. Eliseev, *Phys. Rev. B*, 2007, **76**, 014102.
15 E. A. Eliseev, A. V. Semchenko, Y. M. Fomichov, M. D. Glinchuk, V. V. Sidsky, V. V. Kolos; Yu. M. Pleskachevsky, M. V. Silibin, N. V. Morozovsky and A. N. Morozovska, *J. Appl. Phys*., 2016, **119**, 204104.
16 I. S. Golovina, V. P. Bryksa, V. V. Strelchuk, I. N. Geifman and A. A. Andriiko, *J. Appl. Phys*., 2013, **113**, 144103.
17 E. A. Eliseev, M. D. Glinchuk, V. V. Khist, C.-W. Lee, C. S. Deo, R. K. Behera and A. N. Morozovska, *J. Appl. Phys*., 2013, **113**, 024107.
18 H. Huang, C. Q. Sun and P. Hing, *J. Phys.: Condens. Matter*, 2000, **12**, L127-L132.
19 A. N. Morozovska, I. S. Golovina, S. V. Lemishko, A. A. Andriiko, S. A. Khainakov and E. A. Eliseev, *Phys. Rev. B*, 2014, **90**, 214103.
20 R. Kretschmer and K. Binder, *Phys. Rev. B*, 1979, **20**, 1065-1076.
21 B. G. Stephenson and M. J. Highland, *Phys. Rev. B*, 2011, **84**, 064107.
22 M. D. Glinchuk, E. A. Eliseev and A. N. Morozovska, *Ferroelectrics*, 2016, **500**, 90-98.
23 S. Li, J. Eastman, Z. Li, C. Foster, R. Newnham and L. Cross, *Phys. Lett. A*, 1996, **212**, 341-346.
24 G. Catalan, B. Noheda, J. McAneney, L. J. Sinnamon and J. M. Gregg, *Phys. Rev. B*, 2005, **72**, 020102(R). B. Wanga and C. H. Woo, *J. Appl. Phys*., 2005, **97**, 084109.
25 J. Paul, T. Nishimatsu, Y. Kawazoe and U. V. Waghmare, *Phys. Rev. Lett*., 2007, **99**, 077601.
26 D. G. Schlom, L.-Q. Chen, C.-B. Eom, K. M. Rabe, S. K. Streiffer and J.-M. Triscone, *Annu. Rev. Mater. Res*., 2007, **37**, 589–626.
27 A. K. Tagantsev, G. Gerra and N. Setter, *Phys. Rev. B*, 2008, **77**, 174111.
28 O. G. Maksimova, A. V. Maksimov and O. S. Baruzdina, *J. Adv. Dielect*., 2017, **7**, 1750004.
29 J. E. Spanier, A. M. Kolpak, J. J. Urban, I. Grinberg, L. Ouyang, W. S. Yun, A. M. Rappe and H. Park, *Nano Letters*, 2006, **6**, 735-739.
30 A. N. Morozovska, E. A. Eliseev and M. D. Glinchuk, *Phys. Rev. B*, 2006, **73**, 214106.
31 I. I. Naumov, L. Bellaiche and H. Fu, *Nature*, 2004, **432,** 737-740.
32 R. Qiu, E. Bousquet and A. Cano, *EPL*, 2015, **112,** 37006.
33 I. S. Golovina, S. P. Kolesnik, I. N. Geifman and A. A. Andriiko, *Ferroelectrics*, 2011, **416**, 133-138.
34 I. S. Golovina, S. P. Kolesnik, V. Bryksa, V. V. Strelchuk, I. B. Yanchuk, I. N. Geifman, S. A. Khainakov, S. V. Svechnikov and A. N. Morozovska, *Physica B*, 2012, **407**, 614-623.
35 I. S. Golovina, B. D. Shanina, S. P. Kolesnik, I. N. Geifman and A. A. Andriiko, *J. Appl. Phys.*, 2013, **114**, 174106.
36 S. Lee, Z.-K. Liu, M.-H. Kim and C. A. Randall, *J. Appl. Phys*., 2007, **101**, 054119.
37 W. P. Chen, Z. J. Shen, S. S. Guo, K. Zhu, J. Q. Qi, Y. Wang and H. L. W. Chan, *Physica B*, 2008, **403**, 660-663.
38 S. Lee, G. A. Rossetti, Jr., Z.-K. Liu and C. A. Randall, *J. Appl. Phys*., 2009, **105**, 093519.
39 C. Ma and A. Navrotsky, *Chem. Mater*., 2012, **24**, 2311−2315.
40 H. H. Sønsteby, H. Fjellvåg and O. Nilsen, *Adv. Mater. Interfaces*, 2017, **4**, 1600903.
41 A. V. Plokhikh, M. Falmbigl, I. S. Golovina, A. R. Akbashev, I. A. Karateev, M. Y. Presnyakov, A. L. Vasiliev and J. E. Spanier, *ChemPhysChem*, 2017, **18**, 1966-1970.
42 M. Falmbigl, I. A. Karateev, I. S. Golovina, A. V. Plokhikh, T. C. Parker, A. L. Vasiliev and J. E. Spanier, *Nanoscale*, 2018, **10**, 12515.
43 K. Sakayori, Y. Matsui, H. Abe, E. Nakamura, M. Kenmoku, T. Hara, D. Ishikawa, A. Kokubu, K. Hirota and T. Ikeda, *Jpn. J. Appl. Phys*., 1995, **34**, 5443–5445.
44 L. Akselrud and Y. Grin, *J. Appl. Crystallogr*., 2014, **47**, 803–805.
45 Z. Zhao, V. Buscaglia, M. Viviani, M. T. Buscaglia, L. Mitoseriu, A. Testino, M. Nygren, M. Johnsson and P. Nanni, *Phys. Rev. B*, 2004, **70**, 024107.
46 C. A. Randall, D. E. McCauley and D. P. Cann, *Ferroelectrics*, 1998, **206-207**, 325-335.
47 B. A. Strukov, S. T. Davitadze, S. G. Shulman, B. V. Goltzman and V. V. Lemanov, *Ferroelectrics*, 2004, **301**, 157-162. M. T. Buscaglia, M. Viviani, V. Buscaglia, L. Mitoseriu, A. Testino, P. Nanni, Z. Zhao, M. Nygren, C. Harnagea, D. Piazza and C. Galassi, *Phys. Rev. B*, 2006, **73**, 064114.
48 C. Bergman, A. Ashkin, A. A. Ballman, J. M. Dziedzic, H. J. Levinstein and R. C. Smith, *Appl. Phys. Lett.*, 1968, **12**, 92-94.
49 I. A. Santos and J. A. Eiras, *J. Phys.: Condens. Matter*, 2001, **13**, 11733.
50 G. V. Lewis and C. R. A. Catlow, *Radiat. Eff.*, 1983, **73** [1-4], 307–314.
51 G. V. Lewis and C. R. A. Catlow, *J. Phys. Chem. Solids*, 1986, **47**, 89–97.
52 D. A. Freedman, D. Roundy and T. A. Arias, *Phys. Rev. B*, 2009, **80**, 064108.
53 E. Chason and P. R. Guduru, *J. Appl. Phys*., 2016, **119**, 191101.
54 E. Vasco and C. Polop, *Phys. Rev. Lett*., 2017, **119**, 256102.
55 M. Yashima, T. Hoshina, D. Ishimura, S. Kobayashi, W. Nakamura, T. Tsurumi and S.Wada, *J. Appl. Phys*., 2005, **98**, 014313.
56 K. Tsuzuku and M. Couzi, *J. Mater. Sci.*, 2012, **47**, 4481–4487.
57 Y. K. V. Reddy, D. Mergel, S. Reuter, V. Buck and M.Sulkowski, *J. Phys. D.: Appl. Phys*., 2006, **39**, 1161–1168.
58 H. Yamaguchi, H. Uwe, T. Sakudo and E. Sawaguchi, *Journal of the Physical Society of Japan*, 1987, **56**(2), 589-595.
59 A. Scalabrin, A. S. Chaves, D. S. Shim and S. P. S. Porto, *Phys. Status Solidi B*, 1977, **79**, 731-742.
60 O. A. Maslova, F. V. Shirokov, Yu. I. Yuzyuk, M. El. Marssi, M. Jain, N. Ortega and R. S. Katiyar, *Physics of the Solid State*, 2014, **56**, 310–316.
61 I. S. Golovina, V. P. Bryksa, V. V. Strelchuk and I. N. Geifman, *Functional materials*, 2013, **20**, 75-80.
62 C. J. Hawley, L. Wu, G. Xiao, I. Grinberg, A. M. Rappe, P. K. Davies and J. E. Spanier, *Phys. Rev. B*, 2017, **96**, 054117.

sentence of text (maximum 20 words) highlighting the novelty of the work:

We demonstrate a novel approach for tuning the ferroelectric phase transition in nanograined thin films utilizing enhanced cation solubility.